

Article

Effect of External Compression on the Thermal Runaway of Lithium-Ion Battery Cells during Crush Tests: Insights for Improved Safety Assessment

Alexander Hahn ^{1,2,*}, Stefan Doose ^{1,2} , Daniel Saathoff ^{1,2} and Arno Kwade ^{1,2} 

¹ Institute for Particle Technology, Technische Universität Braunschweig, Volkmaroder Straße 5, 38104 Braunschweig, Germany

² Battery LabFactory Braunschweig, Technische Universität Braunschweig, Langer Kamp 19, 38106 Braunschweig, Germany

* Correspondence: alexander.hahn@tu-braunschweig.de; Tel.: +49-531-391-94675

Abstract: To gain better understanding of the safety behavior of lithium-ion batteries under mechanical stress, crush tests are performed and reported in literature and in standards. However, many of these tests are conducted without the use of a cell clamping device, whereas external pressure is applied to the cell in a battery module in applications such as in an electric vehicle. The objective of this manuscript is to determine the effect of differing external compression on the thermal runaway of battery cells. Therefore, in this study, crush tests are performed with a hemispherical punch in a battery cell test chamber on commercially available 5 Ah pouch cells in a clamping device at four different normal stresses. The results are compared to cells that are free to expand with gas evolution. It is shown that applying compression to the cells not only results in a greater reproducibility of the experiments but that it also affects the thermal runaway process itself. With decreasing clamping stresses, the reaction time of the thermal runaway is increased by up to 19%, and the mass ejection is decreased by up to 10%, which, in turn, strongly influences the measurable gas concentrations by up to 80%. Based on this, a defined clamping compression was selected to obtain comparable results for different cell formats.

Keywords: lithium-ion battery; crush test; mechanical abuse; thermal runaway; safety; hazard potential; clamping device; short circuit



Citation: Hahn, A.; Doose, S.; Saathoff, D.; Kwade, A. Effect of External Compression on the Thermal Runaway of Lithium-Ion Battery Cells during Crush Tests: Insights for Improved Safety Assessment. *Batteries* **2023**, *9*, 404. <https://doi.org/10.3390/batteries9080404>

Academic Editor: Wojciech Mrozik

Received: 14 June 2023

Revised: 17 July 2023

Accepted: 28 July 2023

Published: 2 August 2023



Copyright: © 2023 by the authors. Licensee MDPI, Basel, Switzerland. This article is an open access article distributed under the terms and conditions of the Creative Commons Attribution (CC BY) license (<https://creativecommons.org/licenses/by/4.0/>).

1. Introduction

Lithium-ion batteries are the main battery technology as an energy storage for portable electronics and electric vehicles because of their high energy density, long cycle life, and low self-discharge rate [1–3]. However, the increasing energy density and reactive nature of lithium-ion batteries is a challenge, as it can also pose a safety risk under certain conditions, such as overcharging, overheating, or physical damage [4–6]. The result can be a thermal runaway, which is defined as a rapid and uncontrolled increase in temperature. It can be triggered by a defect or external stress, which initiates a chain reaction that causes a rapid temperature increase in the battery [7,8]. The high temperature can then lead to further degradation of the battery components, which generates more heat and enhances the temperature increase. The thermal runaway reaction in a lithium-ion battery starts with the decomposition of the solid electrolyte interface (SEI) at relatively low temperatures between 60 and 120 °C [5,9,10]. This initial step sets off a chain reaction that involves the incorporation of the liquid electrolyte and its interaction with the conducting salt, the anode components, and the intercalated lithium. The reaction between the liquid electrolyte and these components releases heat and causes the temperature to rise within the battery [4,11]. If a typical separator made of polypropylene (PP) and polyethylene (PE) is used, the separator starts to melt at temperatures of about 165 °C (PP) and 135 °C

(PE), creating a short-circuit surface between the electrodes [4,9,12]. As the temperature continues to increase, the cathode active material begins to decompose at temperatures above 250 °C [9]. This process can result in swelling of the battery, the release of flammable and toxic gases, and, in severe cases, a fire or explosion [4,13].

One way to evaluate battery safety is to perform crush tests, as they assess the ability of a battery to withstand physical stress and abuse [14–16]. To simulate the effects of mechanical damage that may occur during normal use or transportation, an external load is applied to the battery during a crush test. These tests can be performed in the out-of-plane direction to analyze the limits of the mechanical properties of the electrodes and separator [17], and in the in-plane direction to analyze the buckling behavior of the battery cell [18]. The results help to determine the integrity of a battery cell or a battery system, as well as its ability to prevent the release of flammable gases or other hazardous materials in the event of physical damage.

The safety of lithium-ion batteries is also governed by a number of industry standards and guidelines [19]. These standards cover a number of aspects, including reliability under different conditions and the test procedures used to assess its safety. When testing single cells, cell clamping is usually not specified, which means that battery cells can expand if gas is generated. In practical applications like an electric vehicle, however, the single cell is located in a rigid battery module or directly in a battery system, where the cell is compressed. Under such conditions, there is no space for volume expansion of the pouch cells. As cells expand during charging and undergo irreversible thickness growth during their lifetime as part of the aging process, the compression in the rigid module consequently increases [20,21]. Therefore, from an application perspective, it is important to analyze the potential differences in thermal runaway at different compressions.

In research, cell clamping is often used for safety tests on pouch cells to increase the reproducibility of experiments [7,22–25]. Examples of such test setups include studies by Stein et al., who used cell clamping for overcharge tests [24]; Doose et al., who used it to investigate thermal runaways of pouch cells with different numbers of electrode layers during nail penetration [25]; and Essl et al., who compared thermal runaway during three different abuse tests: overtemperature, overcharge, and nail penetration [7]. In this study, springs were used to compress each cell between two plates. Höschele et al. [26] examined the impact of preload force and state of charge (SOC) on the mechanical behavior and failure behavior of constrained and unconstrained pouch cells during mechanical abuse testing. They found that internal stress from preload forces and reversible swelling impact the failure behavior of pouch cells. Applying pre loads resulted in an earlier failure and a thermal runaway with high internal pressure, leading to directed out-gassing. However, there has been no study in which the effect of different clamping compressions on thermal runaways has been investigated. In thermal runaway research, gas analysis is frequently employed to assess the chemical reactions occurring within the cell during a thermal runaway, as it allows for a detailed analysis of the processes taking place, depending for instance on the trigger that led to the thermal runaway [7]. Nevertheless, the existing research does not suggest any alteration in the measurement outcomes with different cell compressions. Thus, in this study, the influence of a cell clamping device with four different normal stresses in crush tests of lithium-ion batteries is investigated. A comparison is made between the results obtained from the clamped and the unclamped cells. The results of the study will elucidate the extent to which thermal runaway is affected by this external influence on the battery cell. Furthermore, this research offers valuable recommendations on conducting experiments in order to obtain consistent and reproducible results.

2. Materials and Methods

The results presented in this study were performed in a specially designed test chamber. At least three tests were performed for each test parameter investigated. The respective mean values were calculated and marked with the corresponding standard deviations.

2.1. Battery Cell Investigation Chamber

The test chamber used was based on the design by Diekmann et al. [22]. However, a newly constructed chamber with additional features was used in this study. The basic structure was a T-shaped stainless-steel tube with a volume of about 47 L, an internal diameter of approximately 310 mm, and a length of 508 mm. It was sealed at all three openings, as shown in Figure 1a. One opening of the chamber had an additional observation window to allow for visual observation of the test runs. A movable base that provided a flat surface for positioning test specimens was situated in the center of the chamber. A high force electro-thrust cylinder with a maximum force generation of 25 kN was mounted on top of the chamber. The electro-thrust cylinder pushed a guide rod sealed to the top cover into the test chamber. A thread was cut into the bottom of this rod to allow any penetration geometry, such as a nail or punch, to be attached. In this study, a hemispherical punch with a diameter of 10 mm was used, which moved at a speed of 1 mm min^{-1} . A compression load cell with a capacity of up to 20 kN was mounted between the electro-thrust cylinder and the guide rod to quantify the load applied to the test object (battery cell). In addition, the ambient temperature in the chamber was measured with a PT100 RTD sensor, and the ambient pressure was measured with a pressure transmitter. The cell voltage of the investigated test cell was sampled using alligator clips, and the temperature on the surface of the cells was measured at two positions using type K thermocouples.

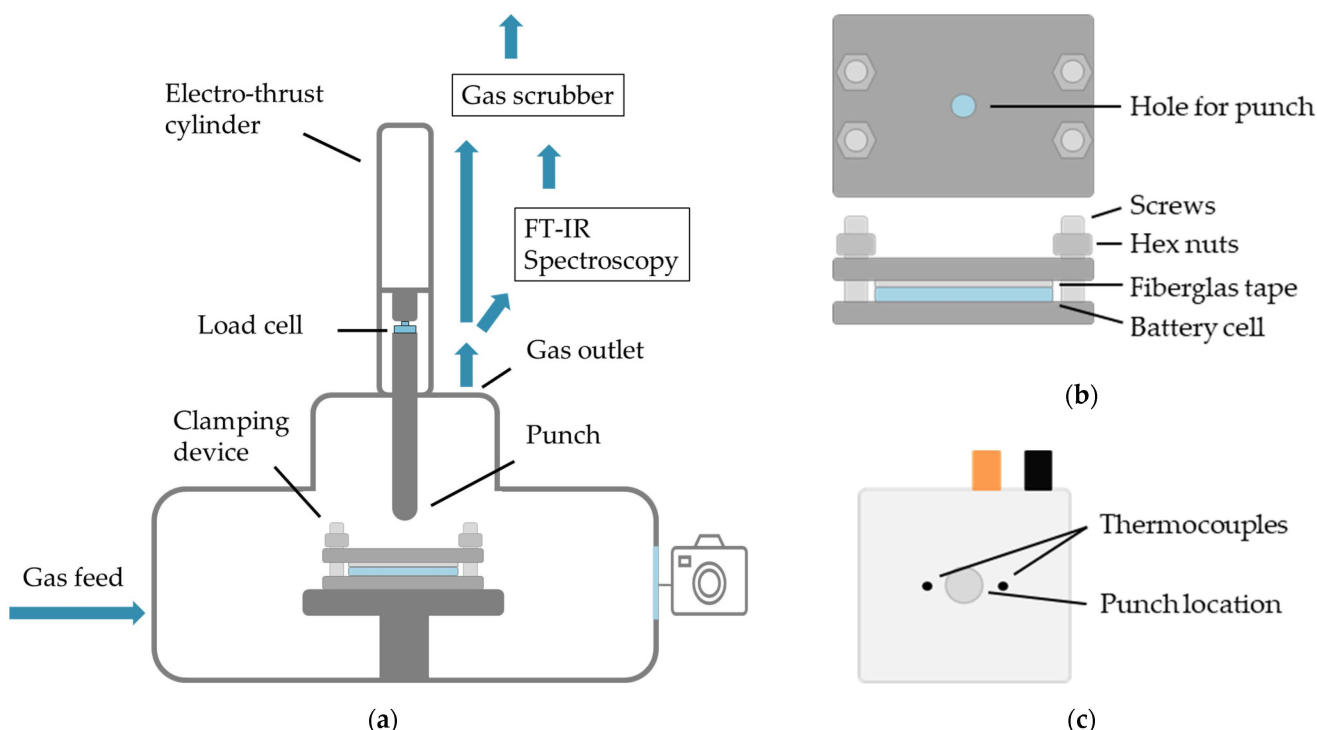


Figure 1. Visualization of the test setup: (a) test chamber with illustration of the cell clamping device and the electric cylinder, including the penetration tool and the gas flow; (b) cell press with the battery cell and insulation material; (c) cell with positioning of the thermocouples.

Prior to the experiments, a defined atmosphere was created in the chamber via an opening on the left side of the chamber. To use an inert carrier gas for downstream gas analysis, in this study, the chamber was flushed with a constant flow of nitrogen gas at 6 L min^{-1} . Behind the gas outlet, the gas was continuously aspirated by a Fourier-Transformation Infrared Spectroscopy (FT-IR) through a heated hose (180°C) and a heated filter with a pore diameter of 3 mm at a flow rate of 6 L min^{-1} . However, as a lot of gas is generated during the thermal runaway, the gas analyzer must be protected from overpressure. Therefore, part of the exhaust gas was routed directly towards the gas scrubber. The FT-IR used an

active nitrogen dilution system that allowed resolution of the infrared active gases even at high gas concentrations. Software provided by the manufacturer compared the recorded spectra with reference spectra at the appropriate wavelengths. The corresponding gas concentrations were determined for each 6 s measurement interval. The gases investigated in this study were carbon dioxide (CO_2), carbon monoxide (CO), methane (CH_4), ethylene (C_2H_4), ethane (C_2H_6), hydrogen fluoride (HF), ethylene carbonate (EC), and ethyl methyl carbonate (EMC).

2.2. Investigated Cells

The battery cells investigated in this study were commercially available battery cells from Kokam Co., Ltd. (Siheung, Republic of Korea) with a capacity of 5 Ah (SLPB50106100). All cells were from the same batch and were subjected to an input test by Ryll et al. [27]. According to the manufacturer, the cell contained a high-energy NMC as the cathode active material and graphite as the anode active material. In addition, the electrolyte used was a mixture of EC, EMC, and LiPF_6 . One cell measured 102 mm × 107 mm and weighed approximately 120 g. All cells tested were charged with 0.1 C to 4.2 V (CC-CV to 0.05 C) at 20 °C prior to testing.

2.3. Cell Clamping

Figure 1b shows an illustration of the cell press used in this study. It consisted of two 10 mm thick plates, which were bolted together with four hex screws. The screws were recessed into the underside of the plate so that the screw heads did not act as a base. Otherwise, the lower plate would be subjected to bending stress at higher loads during the crush test, causing possible elastic or plastic deformation and thus affecting the force–displacement curves of the crush test. The cell was centered on the lower plate, and the thermocouples were taped 2 cm from the center to the cell surface, as shown in Figure 1c. A fiberglass tape was placed on top of the cell to prevent the thermocouples from being pressed into the cell by the contact pressure of the two plates and to provide thermal insulation between the thermocouples and the top plate. From a thermal standpoint, it would also make sense to use the fiberglass tape under the cell, but this would affect the force–displacement curve of the crush test. The top plate was placed on top of the fiberglass tape and had a center hole that was 3 mm larger in diameter than the 10 mm diameter punch selected for this study. A hole of the same size was cut in the fiberglass tape under the hole of the top plate so that the punch was in direct contact with the cell. Four nuts and washers were used on the top to adjust the clamping compression by torque. In this study, normal stresses of 0.05 MPa, 0.15 MPa, 0.25 MPa, and 0.50 MPa were compared to cells that could expand freely during the thermal runaway. In this case, the cell was placed directly on the movable base in the test chamber with the thermocouples taped to the top of the cell.

2.4. Visual Analysis

In order to monitor the tests, the test procedure was recorded through the viewing window of the test chamber. After the tests, photographs of the discharged battery cells were taken to document any damaged areas, cell openings, and other anomalies. X-ray images of selected cells were taken from the crushed side of the cells using an X-ray inspection system (X8011-II PCB flex).

3. Results and Discussion

During the crush test, the punch moved into the cell at a constant speed. As the punch touched the cell, the force with which the punch pressed into the cell increased, as shown in Supplementary Material Figure S1. Once critical mechanical stresses in the contact area were exceeded, cracks formed in the separator and electrodes. Subsequently, the force dropped as the punch penetrates further into the cell.

When cracks occur in a separator and electrodes, the electrodes touch, forming a conductive connection (i.e., an internal short circuit). This connection allows an electrical

current to flow, causing the battery to discharge. The resulting drop in cell voltage over time is shown in Figure 2 as a function of the relative test time. The time has been zeroed to the time at which the short circuit occurred. The cell voltage starts at approximately 4.2 V, which corresponds to a SOC of 100%. A sharp voltage drop occurs at 0 s relative test time. This initial voltage drop results in a voltage below 1.5 V for the cells with clamping stress from 0.05 MPa to 0.25 MPa. For the highest compressed cell, the voltage drops only to 2.2 V, whereas the voltage drops to 2.57 V for the unclamped cell. Over a period of about 2 s, the cell voltage decreases at a much slower rate and with increased standard deviation. As soon as a voltage drop occurs, Joule heat is generated due to the high local current flow [28]. When the critical temperature for the used material is exceeded, a chemical chain reaction with various exothermic reactions is initiated. The reaction products of these reactions are, in addition to solids, mostly gaseous and cause an associated particle detachment of the coating from the current collector foils. Both gas formation and particle detachment increase the short-circuit resistance between the electrodes themselves and between the punch and the electrodes. Due to the resulting lower current flow in the short-circuit region, the cell voltage relaxes for a short period with a high standard deviation.

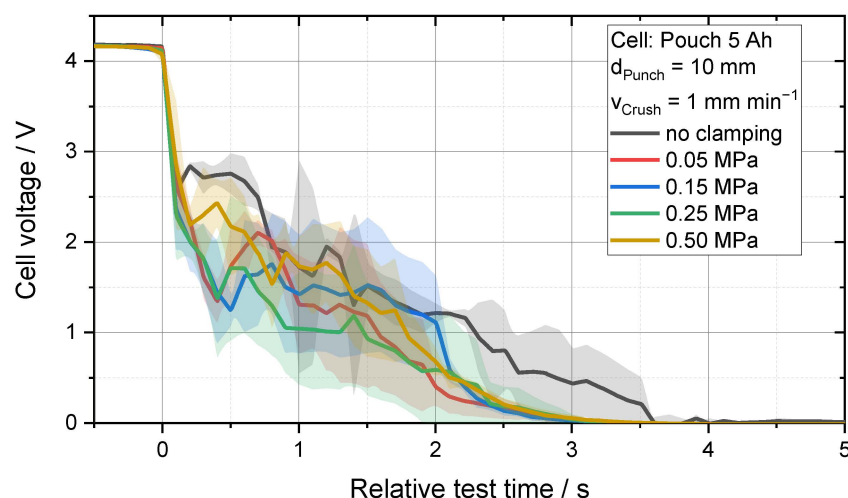


Figure 2. Comparison of the cell voltage as a function of the relative test time during crush tests of battery cells at different clamping normal stresses.

At a relative test time of 3 s, the standard deviation decreases again significantly for all clamped cells. These cells reach 0.05 V at a relative test time of 3.52 s, which corresponds to an almost complete discharge of the cell. The unclamped cells have a 19% longer voltage drop. The longer discharge time as well as the higher standard deviation can be explained by the strong inflation of the cells. As gas is generated, the pressure in the cell increases, causing the pouch foil to expand and push the electrode layers apart. The increased electrode spacing also increases the reaction paths in the cell, resulting in a slower discharge. Since cell inflation and electrode drift are not very reproducible, the standard deviation also increases. As the electrode layers move, heat transfer and reaction propagation change. It can be concluded that cell clamping stabilizes the cell structure and results in a lower short-circuit resistance during the reaction. Furthermore, a higher reproducibility due to cell clamping is evident.

The cell surface temperatures resulting from Joule heating and exothermic reactions are shown in Figure 3. The lowest maximum temperatures were measured at $312.2\text{ }^{\circ}\text{C} \pm 82\text{ }^{\circ}\text{C}$ for the unclamped cells. Due to the non-reproducible inflation of the cells, the thermocouples moved away from the reaction center, reducing both the measured maximum temperature and the measuring accuracy. With clamped cells, the external compression prevented expansion of the pouch bag. The thermocouples remained close to the reaction center, allowing for more reproducible temperature measurements. The highest surface

temperatures of $540.5^{\circ}\text{C} \pm 19.3^{\circ}\text{C}$ were measured for the cell with the lowest clamping normal stress (0.05 MPa). As the clamping stress increased, the maximum temperature decreased from $533.1^{\circ}\text{C} \pm 23.5^{\circ}\text{C}$ at 0.15 MPa, to $512.6^{\circ}\text{C} \pm 25.9^{\circ}\text{C}$ at 0.25 MPa, and then $508.8^{\circ}\text{C} \pm 9.7^{\circ}\text{C}$ at 0.5 MPa. As the clamped cells were only thermally insulated from the stainless-steel plates on the top side, heat transfer was enhanced on the bottom side. Due to the high thermal mass of the bottom plate compared to the cell, a cooling effect occurred. This can also be seen in the curve in Figure 3. The curves representing cells under higher normal stresses appear at lower temperatures than those representing cells at lower stresses. For the unclamped cell, the maximum temperature is significantly lower, and the temperature drop is noticeably slower. This is because the pouch bag loses surface contact with the bottom plate as the cell inflates, which reduces heat transfer. Thus, after 100 s, the temperature of the unclamped cells is still 68.6% of the maximum temperature ($214.2^{\circ}\text{C} \pm 56^{\circ}\text{C}$), whereas the cells with the lowest clamping compression showed only 29.1% ($157.5^{\circ}\text{C} \pm 4.1^{\circ}\text{C}$).

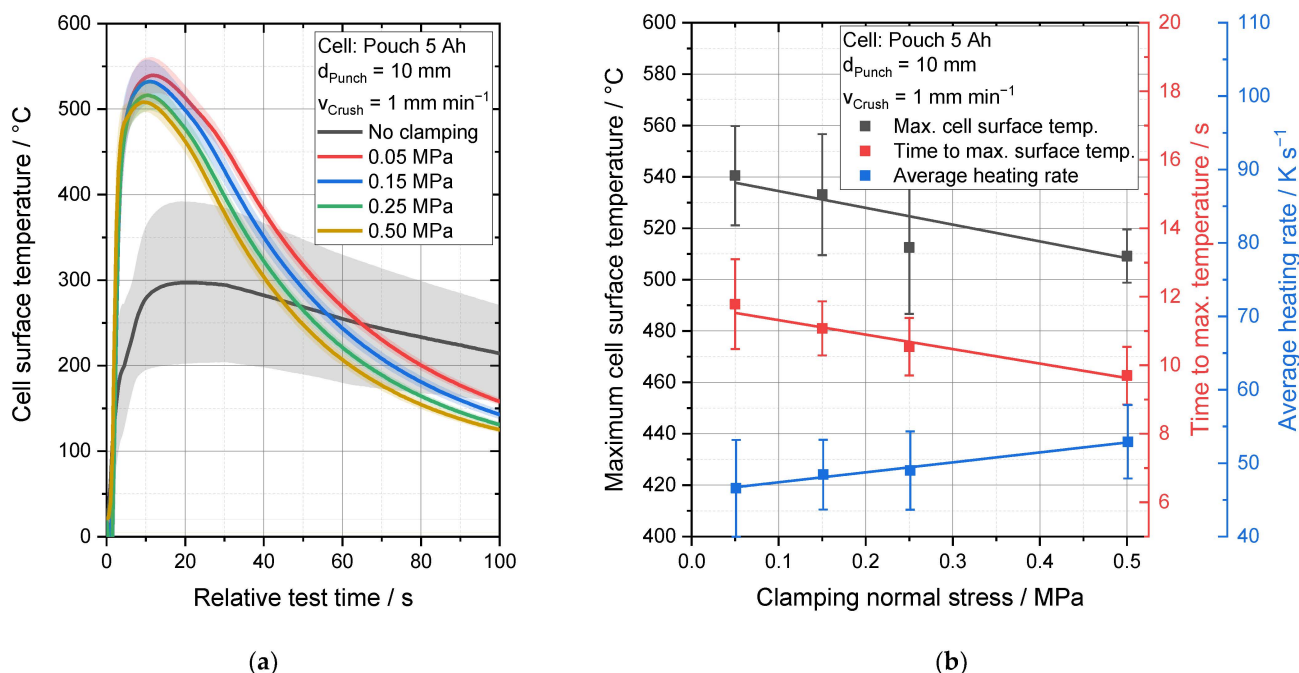


Figure 3. Illustration of the cell surface temperature: (a) Plot of average cell surface temperatures versus time; (b) plot of maximum temperatures, time to maximum temperature, and heating rate after thermal runaway for the applied clamping normal stresses.

Cell clamping also affects the time until the maximum temperature is reached. Based on the maximum temperature and the time, the heating rate can be calculated, as shown in Figure 3b. Due to the large differences in the maximum temperature, the unclamped cells are not shown here. A higher clamping compression means that the electrode layers have a smaller distance between them, allowing the heat to spread through the cell more quickly. The average heating rate has been identified as an indicator of heat propagation in the cell. It indicates the average temperature rise per second from the time of the initial voltage drop until the maximum temperature is reached. For the cells with a clamping stress of 0.05 MPa, this value corresponds to $46.6\text{ K s}^{-1} \pm 6.6\text{ K s}^{-1}$. This value increases linearly through $48.4\text{ K s}^{-1} \pm 4.8\text{ K s}^{-1}$ and $49\text{ K s}^{-1} \pm 5.3\text{ K s}^{-1}$ at 0.15 MPa and 0.25 MPa to $52.9\text{ K s}^{-1} \pm 5\text{ K s}^{-1}$ at 0.5 MPa cell clamping stress. Thus, for each 0.1 MPa increase in the cell clamping normal stress the heating rate increases by 1.36 K s^{-1} .

Figure 4 shows the maximum load of the punch for an unclamped cell as well as the cells tested with different clamping stresses. The clamping normal stress of 0 MPa corresponds to the theoretical case where the cell is clamped between two plates, but no

forces are applied to the cell from the plates. Therefore, the data for the cells without clamping compression are shown in a separate area of the diagram. It can be seen that the external compression has no statistically significant effect on the maximum loads during the crush test. There is also little difference in the depth of penetration (displacement at maximum load) into the cell for the different parameters. The crush tests in this study use a recess in the top clamping plate for the punch. Thus, the plates only apply forces to the cells in the areas outside the recess. Therefore, the area loaded by the punch has no preload prior to each test. The influence of the external compression on the lateral strain, which could influence the formation of cracks in the separator, cannot be determined.

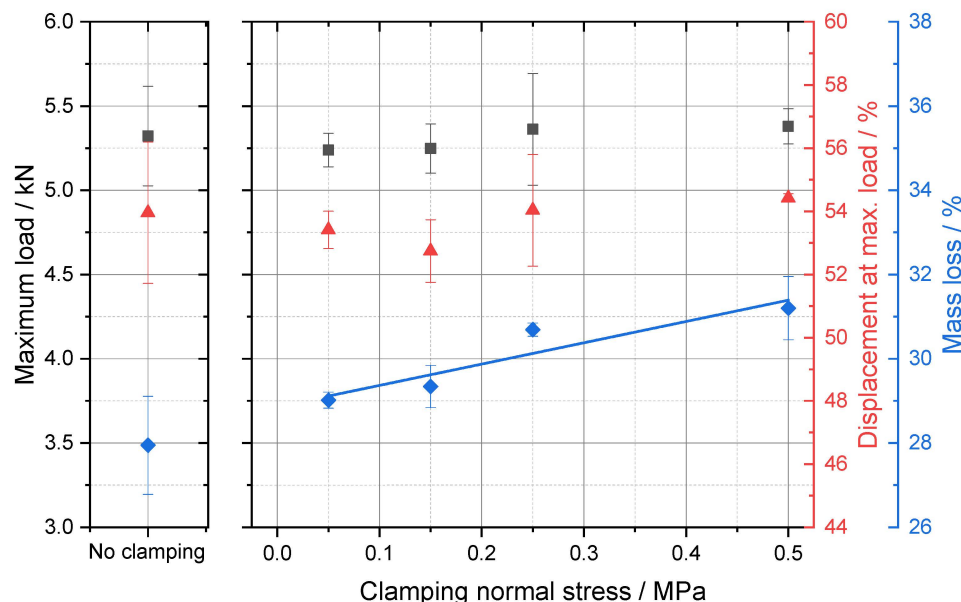


Figure 4. Illustration of the maximum applied load, displacement in percent related to the cell thickness during crush test, and mass loss after thermal runaway for the applied clamping normal stresses.

After thermal runaway, the battery cells experience significant weight loss of up to 31%. This is due to gas generation from the reaction of various cell components and the explosive rupture of the pouch foil and the associated ejection of cell components (particles of the electrode coating and electrolyte). With the high gas generation due to a short circuit in the cell, the pressure inside the cell increases until a tear occurs in the sealing edge of the pouch foil. The gas then flows in the direction of the cell opening created by the tear. However, in the absence of clamping, the mass loss is 1% less than for a cell with the minimum clamping normal stress used in this study, as shown in Figure 4. In addition, these cells have the highest standard deviation of measured mass loss. Figure 5a illustrates that there is less space between the electrodes for the gas to flow through when a higher clamping stress is used. This seems to have an effect on the amount of material that is transported out of the cell during thermal runaway. In the experiments conducted in this study, a slope of 0.5% mass loss is determined per increase in clamping normal stress of 0.1 MPa.

The CT images of the cells in Figure 5b confirm this observation. In the new and untested state, the CT image of the cell body can be seen as a uniform dark black rectangle. After the thermal runaway is completed, various shades of gray are visible. The lighter the shade, the lower the local material density. At a low clamping normal stress, such as 0.05 MPa, the lighter areas are distributed relatively even over the cell area, indicating that the gas is flowing evenly over the electrode surfaces. When the clamping stress is increased to 0.5 MPa, there is only a little space between the electrodes so that gas paths are formed within the cell structure. The coating material and electrolyte is transported out of the cell along these gas paths.

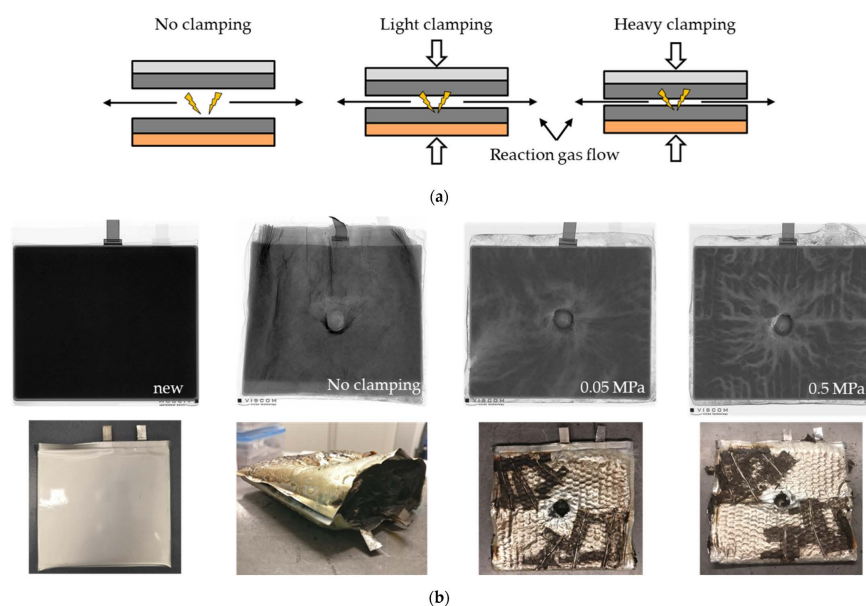


Figure 5. Effects of gas development in a battery cell during thermal runaway: (a) Visualization of gas flow from the cell in the unclamped state compared to light and heavy clamping; (b) X-ray images and photos of battery cells before and after thermal runaway at different clamping stresses.

One way to make this observation measurable is to examine the reaction gases. In Figure 6a, the concentration of CO is plotted against the relative test time. For all test variants, a strong increase in the CO concentration can be observed immediately after the start of the reactions. This process reaches a maximum after about 20 to 30 s. However, since the chamber is continuously flushed with nitrogen, the concentration decreases again over a period of 30 min. The CO gas concentration of the cells without cell clamping reached a maximum of $27,415 \text{ mg m}^{-3}$, about 81% higher than the mean value of the clamped cells. The formation of CO is mainly due to the decomposition of the electrolyte and the reactions of the electrolyte with the anode [23]. As described above, clamped cells experienced a higher ejection of particulate cell components and the electrolyte. Outside the cell, the ejected material cooled and was no longer available for subsequent reactions. Indeed, particulate electrode material with significant moisture could still be found on the walls of the test chamber after the tests were completed. In the case of unclamped cells, the ejected particles are very dry. For these cells, a larger amount of electrolyte remained initially in the cell, which was due to the lower mass ejection. The remaining electrolyte then reacted in a series of different reactions, thus causing such a large difference in gas concentrations.

It is noticeable that the CO concentration also increases with increasing compression after the occurrence of the thermal runaway, as shown in Figure 6b. The maximum concentrations increase from $12,977 \text{ mg m}^{-3} \pm 668 \text{ mg m}^{-3}$ (0.05 MPa) to $14,574 \text{ mg m}^{-3} \pm 1525 \text{ mg m}^{-3}$ (0.15 MPa) and $15,943 \text{ mg m}^{-3} \pm 1936 \text{ mg m}^{-3}$ (0.25 MPa) to $17,175 \text{ mg m}^{-3} \pm 1412 \text{ mg m}^{-3}$ (0.50 MPa). This distribution of the maxima follows an asymptotic regression model given in Equation (1). The factor “a” describes the asymptote at $17,954.8 \text{ mg m}^{-3}$, whereas $(a - b)$ corresponds to the theoretical case of a clamping stress of 0 MPa, where the cell is clamped between two plates, but no forces are applied to the cell from the plates. The values of the variables in this equation are listed in Table 1. It is important to note that this formula has only been empirically evaluated for the limits between 0.05 and 0.5 MPa.

$$y = a - b * c^{\sigma_{cl}/1\text{MPa}}, \quad (1)$$

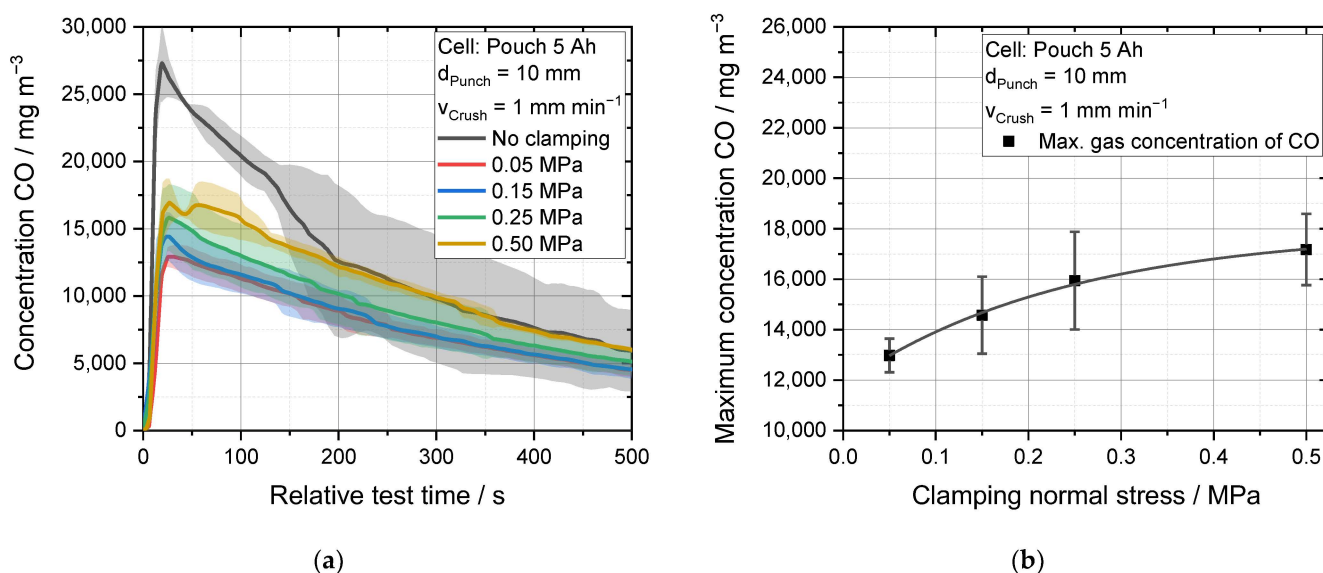


Figure 6. CO gas concentration: (a) Gas concentration versus time after thermal runaway of battery cells at different clamping normal stress; (b) Asymptotic regression model fit of gas concentration peaks at different clamping normal stresses.

Table 1. Variables of the asymptotic regression model describing the maximum gas concentrations of CO, CO_2 and CH_4 as a function of the clamping normal stress.

Variables	CO	CO_2	CH_4
a [mg m^{-3}]	$17,954.8 \pm 4$	$56,124.5 \pm 106.8$	1753.7 ± 2.6
b [mg m^{-3}]	6141.2 ± 31	$16,034 \pm 91.6$	315.5 ± 5.1
c [-]	0.0153 ± 0.015	0.0777 ± 0.003	$2.2 \times 10^{-4} \pm 8.5 \times 10^{-5}$

It is to be expected that the formation of gas paths (Figure 5) at a higher clamping compression limits the ejection of electrolyte mostly to the areas of these pathways. The electrolyte in the other areas of the cell remains in the cell and can therefore participate in various reactions. On the other hand, when a lower clamping compression is used, the electrolyte is expelled from the electrode surface over a larger area. Less electrolyte thus remains in the cell, resulting in lower CO concentrations. This means that the increase in mass loss, shown in Figure 4, is only due to the increased amount of particulate ejection. Consequently, at low clamping compression, a comparatively greater amount of electrolyte and fewer particles were initially ejected, whereas, at high clamping compression, less electrolyte and more particles were ejected. The electrolyte that initially remained in the cell decomposes and reacts with the cell components, as mentioned above. When the reaction is complete, no significant amount of electrolyte is expected to remain in any of the test cells. In the case of an unclamped cell, the cell expands. As a result, there is a lot of space between the electrode layers and the gas can easily escape. Due to this undirected gas ejection, a larger part of the electrolyte initially remains in the cell.

Figure 7 shows the peak concentrations of all measured infrared-active gases in the form of a bar chart. CO_2 , CH_4 , C_2H_4 , and C_2H_6 , like CO, are reaction products of the electrolyte decomposition reaction and the electrolyte reaction with the cell components [29,30]. Therefore, higher concentrations of these reaction products were measured for the unclamped cells. The increase in concentration for CO_2 is very similar to that of CO at about 77% of the mean value of the clamped cells, whereas a much lower increase of about 42% is measured for CH_4 . For different clamping compressions, the same asymptotic regression curve is obtained for CO_2 and CH_4 as for CO, as shown in Table 1. For C_2H_4 , this course deviates slightly, whereas the trend in C_2H_6 follows an up and down movement. As CO_2 and CO are preferentially formed in the decomposition reactions, favorable conditions

may cause the evolution rate of C_2H_4 and C_2H_6 to deviate as an intermediate product of the decomposition reaction. In addition to the decomposition of the electrolyte, it is also converted to a gaseous state and detected in the gas analysis. As higher concentrations of electrolyte decomposition products were measured for the unclamped cells, the concentration of gaseous electrolyte components should, in principle, decrease, as the same amount of reactants were present in all cells. Although the concentration of EMC for unclamped cells is slightly lower, it is significantly higher than expected at $53,814 \text{ mg m}^{-3} \pm 5271 \text{ mg m}^{-3}$ compared to $64,460 \text{ mg m}^{-3} \pm 2324 \text{ mg m}^{-3}$, the mean value of all clamped cells. This observation could be due to an incomplete evaporation of the electrolyte during the thermal runaway, as is evidenced by the moist particulate residue on the wall of the test chamber for the clamped cells. As soon as the ejected wet electrode material touches the wall of the test chamber, it cools down to laboratory ambient temperature. As the boiling point of EMC is 107°C and that of EC is 248°C [31], no further phase change or reactions can take place. As a result, the absolute amount of gas is lower for the clamped cells.

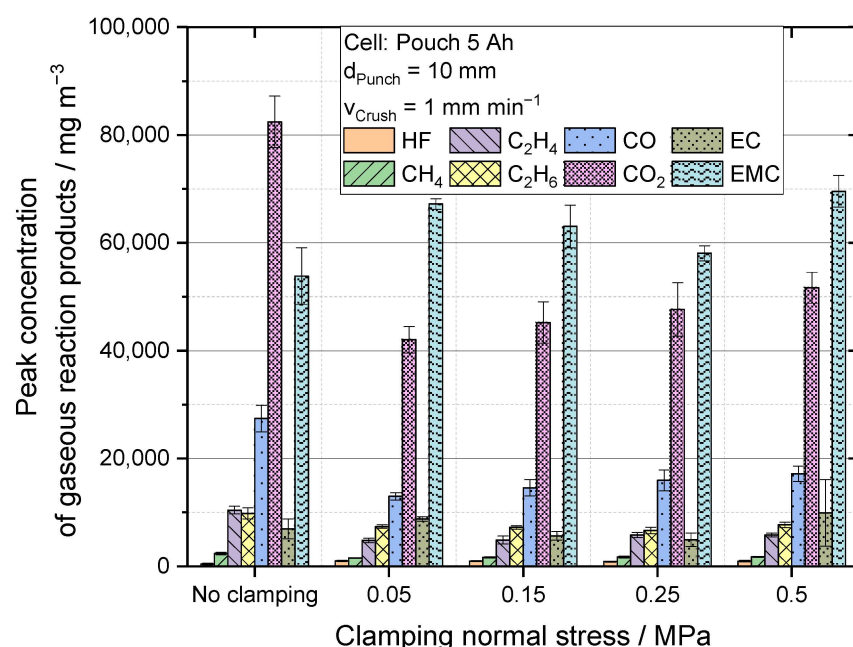


Figure 7. Illustration of the maximum concentrations of the measured infrared active gases during the thermal runaway for different clamping normal stresses.

The concentration of HF remains constant for the clamped cells over the different clamping compressions at about $947 \text{ mg m}^{-3} \pm 112 \text{ mg m}^{-3}$. Only for the unclamped cells, a 54% lower concentration is measured at $438 \text{ mg m}^{-3} \pm 126 \text{ mg m}^{-3}$. The gaseous HF is mainly formed by decomposition of the conductive salt LiPF_6 contained in the electrolyte, starting at temperatures of 80°C , and the PVDF binder contained in the electrodes, starting at around 300°C [10,14]. These temperatures are measured on the surfaces of both the unclamped and clamped cells, so it can be assumed that HF is formed in all cells tested. In addition, the increased electrolyte ejection during thermal runaway of the clamped cells should result in less LiPF_6 remaining in the cell to react to HF. However, as higher HF concentrations were measured for these tests, it appears that the HF tends to react directly without cell clamping due to its high reactivity. After that, measurement in the downstream FT-IR is no longer possible.

The FT-IR analysis shows that significantly higher gas quantities can be measured when no clamping device is used, and, in particular, the electrolyte decomposition products increase while the HF measurable concentration decreases.

The investigations conducted and phenomena identified in this study relate to pouch cells. Both a cylindrical cell and a prismatic cell have a much stronger housing, often made

of aluminum or steel. In addition, both cell types have a safety vent that can prevent severe cell inflation [32,33]. The differences in the measured parameters listed in this study are, therefore, not fully transferable to other cell types and would also need to be evaluated.

In addition, the investigations performed in this study are intended to provide a basis for improving the test performance for investigating thermal runaway. The quasi-static crush test is a test designed to investigate the effects of mechanical deformation under laboratory conditions. In order to simulate real-world scenarios, such as a possible vehicle crash, the indentation speed must be increased. This changes the stiffness and failure behavior of the cell [34,35]. However, the study shows how the cell behaves in a compression range similar to applications such as an electric vehicle. The thickness changes in the battery cell that occur during cycling and aging, which cause an increase in compression in a rigid module, can also affect the thermal runaway characteristics. The results can, therefore, be used as a basis for future module-level thermal runaway simulations.

4. Conclusions

In this study, the influence of clamping compression in mechanical abuse tests was investigated. For this purpose, crush tests were performed in a newly designed battery cell abuse test chamber. The results obtained with a clamping device with four different normal stresses were compared to cells that were free to expand with gas evolution. It can be seen that the external compression on the cells has no influence on the occurrence of a short circuit in the contact area of the punch. For all test parameters, approximately the same maximum load and penetration depth were measured when thermal runaway occurred. However, larger differences are measurable in the reaction process of the thermal runaway.

If not clamped, the cells inflate, which lengthens the reaction path and increases the reaction time. At the same time, cell inflation is less reproducible due to the additional degrees of freedom. In addition, as the cell inflates, the thermocouples used for temperature monitoring move away from the center of the cell, resulting in measurements of lower maximum temperatures. At the same time, the use of a clamping device increases the amount of electrode coating material and electrolyte that was ejected during thermal runaway. The external clamping of the cells compresses the electrode layers, leaving less space for the gas flow, which entrains more material. This leads to significant changes in the concentrations of the escaping reaction gases. While the concentrations of CO₂, CO, and hydrocarbons increase by about 80%, in some cases when no clamping device is used, there are smaller differences in the gaseous electrolyte components and a reduction of more than 50% in the HF concentration.

When comparing different clamping normal stresses, the differences in reaction time are small. Slightly lower maximum temperatures are measured at higher clamping compressions due to increased heat transfer to the metal plates. In addition, the mass ejection from the cell is reduced to channels formed by the gas flow on the electrode structure. This results in a greater amount of electrolyte and electrode components remaining in the cell where they can decompose, thereby increasing the concentrations of CO₂, CO, and hydrocarbons, which asymptotically approach a limit.

This study provides valuable insight into the thermal runaway processes observed during mechanical testing of individual pouch cells with compressions in a range close to the application. While current test standards, such as IEC 62660-2 [36], do not require external clamping during single cell testing, this study confirms that clamping is not necessary to meet these standards, as successful compliance is based on the absence of thermal runaway. The study demonstrates that external clamping does not significantly affect the occurrence of the initial short circuit leading to thermal runaway in crush tests. Moreover, the research highlights the importance of considering the effect of cell clamping on the thermal runaway process, particularly in relation to gas formation. It is recommended that a defined normal stress is selected to ensure the reproducibility of the results. This implies that cells with larger surface areas require higher compression forces to achieve the same normal stress for meaningful comparisons of the results. The authors suggest a clamping

normal stress of 0.15 MPa as an appropriate value to achieve reproducible results with low thermal effects in a range of good cell performance [20]. For a direct comparison to the application, the corresponding clamping stress from the application should be used.

Supplementary Materials: The following supporting information can be downloaded at: <https://www.mdpi.com/article/10.3390/batteries9080404/s1>, Figure S1: Example of selected force-displacement curves of crush tests during indentation with a 10 mm punch at a speed of 1 mm/min at different clamping normal stresses; Figure S2: Asymptotic regression model fit of gas concentration peaks of CO₂ at different clamping normal stresses; Figure S3: Asymptotic regression model fit of gas concentration peaks of CH₄ at different clamping normal stresses; Figure S4: Gas concentration of CO₂ versus time after the thermal runaway at different clamping normal stresses; Figure S5: Gas concentration of HF versus time after the thermal runaway at different clamping normal stresses; Figure S6: Gas concentration of CH₄ versus time after the thermal runaway at different clamping normal stresses; Figure S7: Gas concentration of C₂H₆ versus time after the thermal runaway at different clamping normal stresses; Figure S8: Gas concentration of C₂H₄ versus time after the thermal runaway at different clamping normal stresses; Figure S9: Gas concentration of EMC versus time after the thermal runaway at different clamping normal stresses; Figure S10: Gas concentration of EC versus time after the thermal runaway at different clamping normal stresses.

Author Contributions: Conceptualization, A.H. and S.D.; Methodology, A.H.; Formal analysis, A.H.; Investigation, A.H. and D.S.; writing—original draft preparation, A.H.; writing—review and editing, A.K., S.D., D.S. and A.H.; supervision, A.K. and S.D.; project administration, A.K. All authors have read and agreed to the published version of the manuscript.

Funding: This research was funded by the German Federal Ministry for Education and Research within the research project BaSS, grant number 16EMO0318.

Data Availability Statement: The data presented in this study are available in this manuscript and the accompanying Supplementary Materials.

Acknowledgments: The authors thank the German Federal Ministry for Education and Research for the funding of the research project BaSS (Reference No. 16EMO0318). We acknowledge support by the German Research Foundation and the Open Access Publication Funds of Technische Universität Braunschweig. Furthermore, thank you to Mathias Bähr and Markus Moeller from Viscom AG for the preparation of X-ray images of the cells. The authors also thank Uwe Stüwe, Marius Schulz, Detlev Hille, and Alexander Diener for the technical support in the realization of the test setup.

Conflicts of Interest: The authors declare no conflict of interest. The funders had no role in the design of the study; in the collection, analyses, or interpretation of data; in the writing of the manuscript; or in the decision to publish the results.

References

1. Nitta, N.; Wu, F.; Lee, J.T.; Yushin, G. Li-ion battery materials: Present and future. *Mater. Today* **2015**, *18*, 252–264. [[CrossRef](#)]
2. Placke, T.; Kloepsch, R.; Dühnen, S.; Winter, M. Lithium ion, lithium metal, and alternative rechargeable battery technologies: The odyssey for high energy density. *J. Solid State Electrochem.* **2017**, *21*, 1939–1964. [[CrossRef](#)]
3. Lu, L.; Han, X.; Li, J.; Hua, J.; Ouyang, M. A review on the key issues for lithium-ion battery management in electric vehicles. *J. Power Sources* **2013**, *226*, 272–288. [[CrossRef](#)]
4. Wang, Q.; Ping, P.; Zhao, X.; Chu, G.; Sun, J.; Chen, C. Thermal runaway caused fire and explosion of lithium ion battery. *J. Power Sources* **2012**, *208*, 210–224. [[CrossRef](#)]
5. Bandhauer, T.M.; Garimella, S.; Fuller, T.F. A Critical Review of Thermal Issues in Lithium-Ion Batteries. *J. Electrochem. Soc.* **2011**, *158*, R1. [[CrossRef](#)]
6. Chen, Y.; Kang, Y.; Zhao, Y.; Wang, L.; Liu, J.; Li, Y.; Liang, Z.; He, X.; Li, X.; Tavajohi, N.; et al. A review of lithium-ion battery safety concerns: The issues, strategies, and testing standards. *J. Energy Chem.* **2021**, *59*, 83–99. [[CrossRef](#)]
7. Essl, C.; Golubkov, A.W.; Fuchs, A. Comparing Different Thermal Runaway Triggers for Two Automotive Lithium-Ion Battery Cell Types. *J. Electrochem. Soc.* **2020**, *167*, 130542. [[CrossRef](#)]
8. Kovachev, G.; Ellersdorfer, C.; Gstrein, G.; Hanzu, I.; Wilkening, H.M.R.; Werling, T.; Schauwecker, F.; Sinz, W. Safety assessment of electrically cycled cells at high temperatures under mechanical crush loads. *Etransportation* **2020**, *6*, 100087. [[CrossRef](#)]
9. Liu, K.; Liu, Y.; Lin, D.; Pei, A.; Cui, Y. Materials for lithium-ion battery safety. *Sci. Adv.* **2018**, *4*, eaas9820. [[CrossRef](#)]
10. Baakes, F.; Lüthe, M.; Gerasimov, M.; Laue, V.; Röder, F.; Balbuena, P.B.; Kreuer, U. Unveiling the interaction of reactions and phase transition during thermal abuse of Li-ion batteries. *J. Power Sources* **2022**, *522*, 230881. [[CrossRef](#)]

11. Tian, X.; Yi, Y.; Fang, B.; Yang, P.; Wang, T.; Liu, P.; Qu, L.; Li, M.; Zhang, S. Design Strategies of Safe Electrolytes for Preventing Thermal Runaway in Lithium Ion Batteries. *Chem. Mater.* **2020**, *32*, 9821–9848. [[CrossRef](#)]
12. Zhang, S.S. A review on the separators of liquid electrolyte Li-ion batteries. *J. Power Sources* **2007**, *164*, 351–364. [[CrossRef](#)]
13. Essl, C.; Golubkov, A.W.; Fuchs, A. Influence of Aging on the Failing Behavior of Automotive Lithium-Ion Batteries. *Batteries* **2021**, *7*, 23. [[CrossRef](#)]
14. Nedjalkov, A.; Meyer, J.; Köhring, M.; Doering, A.; Angelmahr, M.; Dahle, S.; Sander, A.; Fischer, A.; Schade, W. Toxic Gas Emissions from Damaged Lithium Ion Batteries—Analysis and Safety Enhancement Solution. *Batteries* **2016**, *2*, 5. [[CrossRef](#)]
15. Kim, J.-S.; Lee, D.-C.; Lee, J.-J.; Kim, C.-W. Optimization of Lithium-Ion Battery Pouch Cell for Maximization of Energy Density while Preventing Internal Short Circuit Caused by Separator Failure under Crush Load. *J. Electrochem. Soc.* **2021**, *168*, 30536. [[CrossRef](#)]
16. Sahraei, E.; Campbell, J.; Wierzbicki, T. Modeling and short circuit detection of 18650 Li-ion cells under mechanical abuse conditions. *J. Power Sources* **2012**, *220*, 360–372. [[CrossRef](#)]
17. Sahraei, E.; Meier, J.; Wierzbicki, T. Characterizing and modeling mechanical properties and onset of short circuit for three types of lithium-ion pouch cells. *J. Power Sources* **2014**, *247*, 503–516. [[CrossRef](#)]
18. Zhu, J.; Koch, M.M.; Lian, J.; Li, W.; Wierzbicki, T. Mechanical Deformation of Lithium-Ion Pouch Cells under In-Plane Loads—Part I: Experimental Investigation. *J. Electrochem. Soc.* **2020**, *167*, 90533. [[CrossRef](#)]
19. Ruiz, V.; Pfrang, A.; Kriston, A.; Omar, N.; van den Bossche, P.; Boon-Brett, L. A review of international abuse testing standards and regulations for lithium ion batteries in electric and hybrid electric vehicles. *Renew. Sustain. Energy Rev.* **2018**, *81*, 1427–1452. [[CrossRef](#)]
20. Cannarella, J.; Arnold, C.B. Stress evolution and capacity fade in constrained lithium-ion pouch cells. *J. Power Sources* **2014**, *245*, 745–751. [[CrossRef](#)]
21. Deich, T.; Storch, M.; Steiner, K.; Bund, A. Effects of module stiffness and initial compression on lithium-ion cell aging. *J. Power Sources* **2021**, *506*, 230163. [[CrossRef](#)]
22. Diekmann, J.; Doose, S.; Weber, S.; Münch, S.; Haselrieder, W.; Kwade, A. Development of a New Procedure for Nail Penetration of Lithium-Ion Cells to Obtain Meaningful and Reproducible Results. *J. Electrochem. Soc.* **2020**, *167*, 90504. [[CrossRef](#)]
23. Doose, S.; Hahn, A.; Bredekamp, M.; Haselrieder, W.; Kwade, A. Scaling Methodology to Describe the Capacity Dependent Responses During Thermal Runaway of Lithium-Ion Batteries. *Batter. Supercaps* **2022**, *5*, e202200060. [[CrossRef](#)]
24. Stein, A.; Kehl, D.; Jackmann, C.; Essmann, S.; Lienesch, F.; Kurrat, M. Thermal Electrical Tests for Battery Safety Standardization. *Energies* **2022**, *15*, 7930. [[CrossRef](#)]
25. Doose, S.; Hahn, A.; Fischer, S.; Müller, J.; Haselrieder, W.; Kwade, A. Comparison of the consequences of state of charge and state of health on the thermal runaway behavior of lithium ion batteries. *J. Energy Storage* **2023**, *62*, 106837. [[CrossRef](#)]
26. Höschele, P.; Heindl, S.F.; Erker, S.; Ellersdorfer, C. Influence of reversible swelling and preload force on the failure behavior of a lithium-ion pouch cell tested under realistic boundary conditions. *J. Energy Storage* **2023**, *65*, 107228. [[CrossRef](#)]
27. Ryll, K.; Hoffmann, L.; Landrath, O.; Lienesch, F.; Kurrat, M. Key Figure Based Incoming Inspection of Lithium-Ion Battery Cells. *Batteries* **2021**, *7*, 9. [[CrossRef](#)]
28. Hendricks, C.; Williard, N.; Mathew, S.; Pecht, M. A failure modes, mechanisms, and effects analysis (FMMEA) of lithium-ion batteries. *J. Power Sources* **2015**, *297*, 113–120. [[CrossRef](#)]
29. Gachot, G.; Ribiére, P.; Mathiron, D.; Grugeon, S.; Armand, M.; Leriche, J.-B.; Pilard, S.; Laruelle, S. Gas chromatography/mass spectrometry as a suitable tool for the Li-ion battery electrolyte degradation mechanisms study. *Anal. Chem.* **2011**, *83*, 478–485. [[CrossRef](#)]
30. Onuki, M.; Kinoshita, S.; Sakata, Y.; Yanagidate, M.; Otake, Y.; Ue, M.; Deguchi, M. Identification of the Source of Evolved Gas in Li-Ion Batteries Using [sup 13]C-labeled Solvents. *J. Power Sources* **2008**, *155*, A794. [[CrossRef](#)]
31. Hess, S.; Wohlfahrt-Mehrens, M.; Wachtler, M. Flammability of Li-Ion Battery Electrolytes: Flash Point and Self-Extinguishing Time Measurements. *J. Electrochem. Soc.* **2015**, *162*, A3084–A3097. [[CrossRef](#)]
32. Kong, L.; Li, C.; Jiang, J.; Pecht, M. Li-Ion Battery Fire Hazards and Safety Strategies. *Energies* **2018**, *11*, 2191. [[CrossRef](#)]
33. Kim, J.-H.; Lee, K.-H.; Ko, D.-C.; Lee, S.-B.; Kim, B.-M. Design of integrated safety vent in prismatic lithium-ion battery. *J. Mech. Sci. Technol.* **2017**, *31*, 2505–2511. [[CrossRef](#)]
34. Kisters, T.; Sahraei, E.; Wierzbicki, T. Dynamic impact tests on lithium-ion cells. *Int. J. Impact Eng.* **2017**, *108*, 205–216. [[CrossRef](#)]
35. Raffler, M.; Sinz, W.; Erker, S.; Brunnsteiner, B.; Ellersdorfer, C. Influence of loading rate and out of plane direction dependence on deformation and electro-mechanical failure behavior of a lithium-ion pouch cell. *J. Energy Storage* **2022**, *56*, 105906. [[CrossRef](#)]
36. IEC 62660-2; Secondary Lithium-Ion Cells for the Propulsion of Electric Road Vehicles: Part 2: Reliability and Abuse Testing, 2nd ed. International Electrotechnical Commission (IEC): Geneva, Switzerland, 2018.

Disclaimer/Publisher's Note: The statements, opinions and data contained in all publications are solely those of the individual author(s) and contributor(s) and not of MDPI and/or the editor(s). MDPI and/or the editor(s) disclaim responsibility for any injury to people or property resulting from any ideas, methods, instructions or products referred to in the content.